THE JOURNAL OF
PHYSICAL CHEMISTRY A

Article

pubs.acs.org/JPCA

Classical Dynamics of H_2O Vibrational Self-Relaxation

Matthew Braunstein* and Patrick F. Conforti

Spectral Sciences Incorporated, 4 Fourth Avenue, Burlington, Massachusetts 01803, United States

ABSTRACT: The vibrational self-relaxation rate constants of the (001), (100), (020), and (010) states of H_2O from 295 to 2500 K are calculated, using $\sim 1.6 \times 10^6$ classical trajectories with Gaussian binning for determining product vibrational quantum numbers. The calculations use a new H_2O-H_2O potential surface obtained by fitting 1.25×10^5 ab initio geometry points at the CCSD(T)//cc-pvtz level of theory. The resulting vibrational self-relaxation rate constants are generally within a factor of 2 of the measured data, which are large in magnitude and tend to increase with decreasing temperature. At lower temperatures, the calculations show long-lived (20 ps and longer) H_2O-H_2O collision complexes which accompany vibrational relaxation. Product rotational and translational energy distributions are investigated, and joint vibrational state and molecule-specific relaxation rate constants are presented.

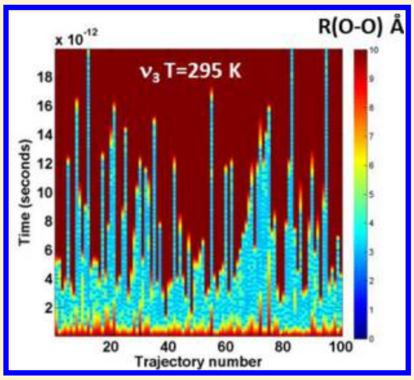

I. INTRODUCTION

Vibrational self-relaxation of H_2O is important in combustion and sound absorption in humid air. Vibrational self-relaxation can be viewed as a probe of the water dimer, a fundamental example of a hydrogen bonded system with at least 10 energy minima[1] and a rich rotational spectrum only recently measured.[2] In 1977, Finzi et al. used laser-excited vibrational fluorescence to measure the rate constants of vibrational self-relaxation of the H_2O $\nu_3 = (001)$, $\nu_1 = (100)$, $2\nu_2 = (020)$, and $\nu_2 = (010)$ states at 293 K.[3] The measured relaxation rate constants were "the fastest which have been measured for any molecule,"[3] orders of magnitude faster than H_2O relaxing by collisions with Ar or O_2 and the general range of observed rate constants for vibrational relaxation processes. In 1989, Zittel and Masturzo measured the vibrational self-relaxation of H_2O from 295 to 1020 K with a similar laser-induced fluorescence technique.[4] They also found large rate constant values. Furthermore, the rate constants for vibrational relaxation increased with decreasing temperature. This "negative temperature dependence" is opposite that of standard models of vibrational relaxation, such as those of Landau and Teller,[5] Parker,[6] and Millikan and White,[7] which are widely used to interpret vibrational kinetics data. Indeed, for H_2O "many of the well-established rules for mechanisms of vibrational relaxation do not apply."[3] Others have noted similar behavior for other hydrogen-containing molecular systems with strong attractions.[8]

Shin modeled the vibrational self-relaxation of H_2O to understand the rate constants.[9] The model used an approximate H_2O-H_2O potential and a semiclassical procedure with ladder operators and a reduced set of dynamical coordinates. The model reproduced the measured self-relaxation probabilities of Zittel and Masturzo[4] and predicted long-lived collision complexes which efficiently transferred energy out of the stretching vibration to bending motion. Recently, Ch'ng et al. used velocity map imaging and classical trajectory simulations to investigate the predissociation of water dimer following vibrational excitation of a local mode water O−H stretch.[10] This related water dimer process also found the stretch-to-bend vibrational pathway to be dominant. We note that a strongly bound collision complex likely plays a key role in the vibrational relaxation of $CH(X^2\Pi, v = 1)$ by N_2 and CO, which is also rapid with a negative temperature dependence.[11]

The present work is a re-examination of the mechanism of H_2O-H_2O vibrational self-relaxation, using a new H_2O-H_2O potential and modern semiclassical methods with the full set of dynamical coordinates. The main goals are to gauge the accuracy of these new procedures and to further understand the dynamics, in particular the nature and role of "collision complexes" and the detailed distribution of energy into both H_2O products. The paper proceeds as follows: Section II describes the new potential which uses $\sim 1.25 \times 10^5$ ab initio geometry points at the CCSD(T)//cc-ptvz level. Section II also describes the classical dynamics method, including the use of Gaussian trajectory weights and the choice of initial conditions for the vibrational relaxation calculations. Section III describes the results of the calculations and compares the results to the rate constant measurements of Zittel and Masturzo.[4] Section III also examines vibrational relaxation mechanisms, including long-lived collision complexes and detailed energy partitioning. Section IV provides conclusions.

II. METHODS

A. Potential Surface. An analytic $H_2O + H_2O$ potential surface was created from $\sim 1.25 \times 10^5$ ab initio geometry points at the CCSD(T) level with a cc-pvtz basis using the Gaussian 03 computer program.[12] The intent was to create a surface accurate up to ~ 100 kcal mol^{-1} above the potential minimum, suitable for examining processes up to 2500 K and for future work at

Received: November 18, 2014
Revised: March 11, 2015

DOI: 10.1021/jp5115527

higher energies. A very rough estimate of the number of geometry points needed assuming 10 geometry points along 12 degrees of freedom (not taking symmetry into account) would be ~10^{12}, which is clearly beyond present-day resources. The strategy adopted in the present study sampled small but important parts of this geometry space. Geometry points were obtained by performing H_2O + H_2O direct dynamics classical trajectory calculations at the semiempirical AM1 level of theory.[13] Geometries along these trajectories were used to compute the CCSD(T)//cc-pvtz ab initio energies, which in turn were fit to an analytic form.

Several batches of AM1 direct dynamics calculations were run. Table 1 shows the initial conditions, spanning a range of initial vibrational, rotational, and translational energy regimes and impact parameters. For each initial condition, at least 100 AM1 direct-dynamics trajectories were run. Using a time step of 1.0 × 10^{-16} seconds, usually every 30th trajectory geometry point was selected for later calculation at the CCSD(T) level. AM1 direct dynamics calculations started at an initial H_2O-H_2O distance of 5 Å and ended when the H_2O-H_2O products were 5 Å apart, so both separated and interacting water geometries were sampled. A few AM1 geometries resulted in O−H bond breaking. The experimental ΔH^0(H−OH) bond energy is 119.2 kcal mol^{-1},[14] but the present focus is on energies below 100 kcal mol^{-1}. Therefore, geometry points where any O−H bonds were greater than 2 Å were removed from the set used for the CCSD(T) calculations.

Table 1. Initial Conditions for AM1 Direct Dynamics Calculations for $H_2O(1)$ + $H_2O(2)$ Collisions[a]

$H_2O(1)$ internal	$H_2O(2)$ internal	translational	impact parameter
(111), T_r = 2000 K	(111), T_r = 2000 K	E_t = 100 kcal mol^{-1}	[0.0:0.2:2.0] Å
(010), T_r = 2000 K	(000), T_r = 2000 K	T_t = 2000 K	[0.0:0.2:2.0] Å
(001), T_r = 2000 K	(000), T_r = 2000 K	T_t = 2000 K	[0.0:0.2:2.0] Å
(242), T_r = 2000 K	(242), T_r = 2000 K	E_t = 50 kcal mol^{-1}	[0.0:0.2:2.0] Å
(111), T_r = 2000 K	(111), T_r = 2000 K	T_t = 2000 K	0.0 Å

[a] The initial vibrational quantum state is given in parentheses, i.e., (ν_1, ν_2, ν_3).

Of the total ~1.25 × 10^5 CCSD(T) geometry energies obtained using this procedure, the CCSD(T) minimum energy point was −1.526 697 08 × 10^2 au and the maximum energy point was −1.523 216 32 × 10^2 au, 218.4 kcal mol^{-1} above this minimum. Figure 1 shows the 2 kcal mol^{-1} binned energy distribution of CCSD(T) ab initio geometry points used in the analytic fit, referenced to the CCSD(T) minimum. The largest part of the distribution is between 10 and 50 kcal mol^{-1}, with most points below 100 kcal mol^{-1}. The distribution of geometries with respect to several internal coordinates, such as the H_2O internal angle and the oxygen−oxygen bond distance, were also checked to confirm these important quantities were being sampled over a wide range and in an even-handed way.

The potential energy surface was constructed using a functional form and fitting procedure described in detail in ref 15. Briefly, this procedure automatically takes into account like-atom symmetry and has proved to be a general and robust method. The general form of the potential is

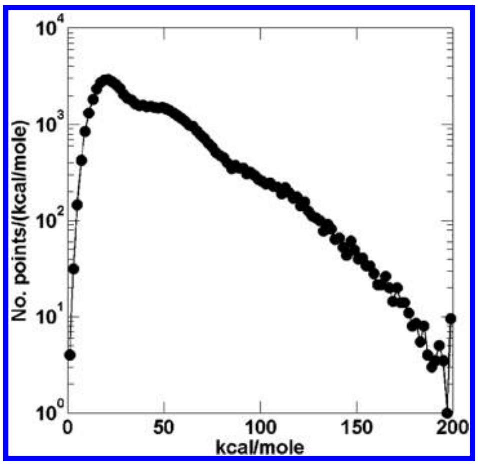

Figure 1. Distribution of energies, in 2 kcal mol^{-1} bins, for the CCSD(T)//cc-pvtz ab initio calculations used in the potential surface fit.

$$V = \sum_{m=0}^{M} D_{abc...o} S[x_{12}^{a} x_{13}^{b} x_{14}^{c} ... x_{56}^{o}]; \quad (m = a + b + c + ... + o) \tag{1}$$

where the basis functions are functions of Morse variables involving the bond distances, r_{ij}, $x_{ij} = \exp(-r_{ij}/a)$. The summation is over all powers of the Morse variables such that the total degree is at most M = 6, 7, or 8. Braams et al. use a unique procedure in which symmetry is taken into account to eliminate redundancies in the potential (shown as the operator S).[15] As a result, a single unknown coefficient ($D_{abc\cdots o}$) appears for each set of (a, b, c, ..., o) that are permutationally equivalent. The permutation group is $S_4 \times S_2$. For the H_2O + H_2O system in this study, this leads to determining 568, 996, and 1676 coefficients for the sixth-, seventh-, and eighth-degree polynomial fits, respectively. The Morse distance parameter, a, was varied from 1.2 to 3.0 au. The optimal root-mean-square fitting value of a = 1.8 au was used. Figure 2a shows the fit results versus the original ab initio data. Figure 2b shows the fit root-mean-square deviation (RMSD) energy error versus the energy above the minimum using sixth-, seventh-, and eighth-degree polynomial fits. The RMSD of the fits gradually increases with energy bin. Below 100 kcal mol^{-1}, the RMSD error for the eighth-degree polynomial fit is less than ~0.5 kcal mol^{-1}. Above 100 kcal mol^{-1}, the RMSD of the fits starts to rise sharply with energy bin.

It was important to ensure the fit also closely represented the 10 known H_2O-H_2O minima. Figure 3a shows comparisons of the present ab initio and eighth-degree polynomial fit results versus literature values from ref 1 with respect to the H_2O-H_2O minimum. The largest error of about 1 kcal mol^{-1} occurs for the separated molecule geometry near 6 kcal mol^{-1}. The ab initio and fit D_e values are 6.16 and 6.30 kcal mol^{-1}, respectively, compared to a literature value of 5.02 kcal mol^{-1} (ref 1). Wang et al. have also found two stationary geometry points for hydrogen exchange ~50 kcal mol^{-1} above the H_2O-H_2O minimum.[16] The fit and ab initio results are within 0.5 kcal mol^{-1} of literature values for these high-energy stationary points. We also conducted a "blind test" of the eighth-order fit by generating about 10 000 geometries from classical dynamics runs using the eighth-order fit potential and the initial conditions of the last row of Table 1. The CCSD(T)//cc-pvtz energies for these blind test trajectory geometry points were

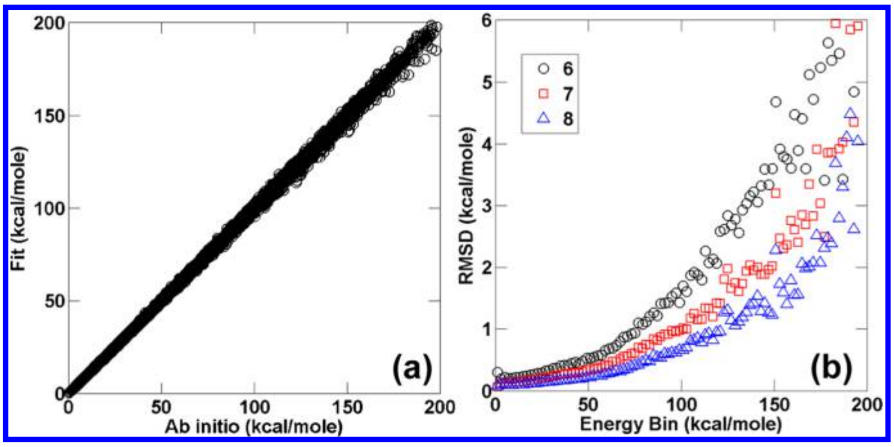

Figure 2. (a) Ab-initio versus eighth-order fit results. (b) Root mean square deviation (RMSD) in 2 kcal mol^{-1} bins versus energy bin for sixth-, seventh-, and eighth-order fits.

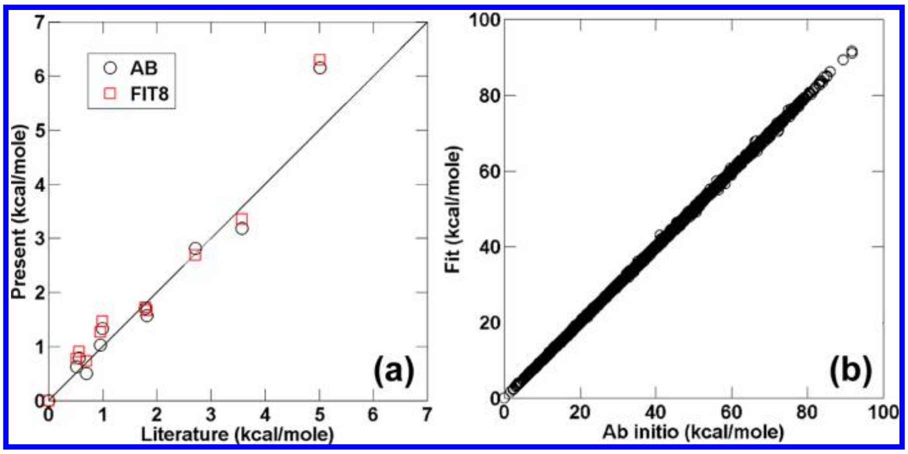

Figure 3. (a) Present results versus the values of Tschumper et al.[1] for the 10 lowest known bound states of water dimer plus two waters far apart with respect to the water dimer global minimum. Ab initio (AB), black circles, and eighth-order (FIT8), red squares, fit results are shown. The black line is perfect agreement to literature values. (b) "Blind test" ab initio versus eighth-order fit results.

then calculated. The fit energies versus the ab initio energies with respect to the ab initio minimum for these blind test geometry points are shown in Figure 3b. There were no outliers, and the RMSD of the fit for these blind points was comparable to the RMSD for the ~1.25×10^5 point training set. The trajectories using this eighth-order fit also had good energy conservation, giving further confidence that the eighth-order fit represented the surface well enough for the intended purpose. The present approach is similar to that of Shank et al., who developed a water dimer potential surface called HBB2.[17] The main difference between the present surface and HBB2 is that the present surface focuses on higher-energy processes, such as highly excited vibrational relaxation at high translational temperatures, and is likely less accurate than the HBB2 surface at lower energies.

B. Classical Dynamics. Classical trajectory calculations were run using the eighth-order fit surface of the CCSD(T)//cc-pvtz geometry points and the dynamics methods described in ref 18. The approach uses standard quasi-classical methods with two important additions: (i) determination of product vibrational quantum numbers through analysis of product momenta and coordinates[19−22] and (ii) a Gaussian binning procedure which weights trajectories based on the closeness of product vibrational energies to discrete quantized values.[23−27] The product vibrational quantum numbers were determined in three ways following ref 18: the harmonic approximation (HA), the elimination method (EM), and the Fourier transform of the action (ACT) method. Results from all methods were similar, and for clarity we will present results using only the EM method. The harmonic vibrational energies from the present surface fit used in the analysis are 3771.2, 1680.9, and 3861.3 cm^{-1} for the ν_1, ν_2, and ν_3 modes, respectively.

In the Gaussian binning procedure a single weight is used for each trajectory (1D-GB).[23−27] For each trajectory, a Gaussian weight is determined for each H_2O product:

$$G(\nu) = \frac{\beta}{\sqrt{\pi}}\exp\left[-\beta^2\left(\frac{(E(\nu') - E(\nu))}{2E(0)}\right)^2\right] \tag{2}$$

In eq 2, $E(\nu')$ corresponds to the energy of a water vibrational state at the end of a trajectory at the noninteger quantum number, ν', $E(\nu)$ corresponds to that energy where the quantum number is the nearest integer value, and $E(0)$ is the zero-point energy. Thus, the quantity $E(\nu') - E(\nu)$ corresponds to the "distance" away from the true integer quantum state. The parameter β is the width of the Gaussian weight and is set to a value of 16.651 so that the width of the weighting function, $G(\nu)$, is 0.1 out of 1.0 (fwhm).

For each trajectory a "joint" weight is also determined, which is a product of the single-molecule Gaussian weights[26]

$$G_{12}(n) = G_1(H_2O(1, \nu))G_2(H_2O(2, \nu)) \tag{3}$$

In eq 3, $(1, \nu)$ denotes the vibrational state of water 1, $(2, \nu)$ denotes the vibrational state of water 2, and (n) denotes the collective vibrational state of the system, where the vibrational states of both waters are specified. Using the joint Gaussian weight, a joint cross section can be defined:

$$\sigma_{12}(n) = \pi b_{\max}^2 \frac{\sum_{p=1}^{N_n} G_{12}(n)}{\sum_{s=1}^{N_s} \sum_{p=1}^{N_{n'}} G_{12}(n')} \tag{4}$$

In eq 4, $b_{\max}$ is the maximum impact parameter, N_n the number of trajectories going to a collective vibrational product state of both waters, (n), and N_s the number of collective vibrational states. We note that recently, several Gaussian binning techniques tailored for analysis of water vibrational states have been published.[28] Because $E(\nu')$ in eq 2 in the EM method includes anharmonic contributions, the present binning procedure is close to the 1GB-H method described in ref 28. The 1GB-EQ method of ref 28, in which $E(\nu)$ of eq 2 is replaced by known quantum state values, promises to provide improved accuracy for very highly excited water products.

The intent is to model the experimental measurements of the $H_2O + H_2O$ vibrational self-relaxation rate constants of Zittel and Masturzo.[4] For these measurements, a laser was used to excite low-lying rotational states of the H_2O $\nu_3 = (001)$ vibrational state in a temperature-controlled flow tube, and the fluorescence decay curves in the 2.7 and 6.3 μm regions were monitored. Assuming a kinetic scheme that will be discussed later, rate constant values were determined from fits to the fluorescence decay curves. Because there was no dependence of the experimental results on the rotational line initially excited and because the rotational level energies were relatively low, ranging from 0.9 to 2.3 kcal mol^{-1}, the present simulations assumed zero temperature in the rotational mode of the initial vibrationally excited $H_2O(1)$. The colliding water, $H_2O(2)$, rotational temperature was set equal to the translational temperature. The following initial conditions were therefore used:

$$\begin{aligned} &H_2O(1, T_r = 0, T_t, \nu) + H_2O(2, T_r = T_t, \nu = 0) \\ &\quad \rightarrow H_2O(1, E_r, E_t, \nu) + H_2O(2, E_r, E_t, \nu) \end{aligned} \tag{5}$$

Four reactant translational temperatures were examined: 295, 500, 1000, and 2500 K. Reactants were initialized with velocities sampled from a Boltzmann translational temperature distribution. For reference, these translational temperatures correspond to $((3/2)k_B T_t)$ energies of 0.88, 1.49, 2.98, and 7.46 kcal mol^{-1}, respectively. The $H_2O(1)$ vibrational states were chosen from the set $\{\nu_1 = (100), \nu_3 = (001), 2\nu_2 = (020), \text{and } \nu_2 = (010)\}$, and the $H_2O(2)$ vibration was set to the ground state. Therefore, there were 16 separate initial conditions batch runs (4 translational temperatures times 4 $H_2O(1)$ initial states). For each of the 16 initial conditions, $\sim 1 \times 10^5$ separate classical trajectories were run, giving a total of $\sim 1.6 \times 10^6$ trajectories. The maximum impact parameter, $b_{\max}$, was 8.0 Å for all calculations. The impact parameter was sampled from a random distribution according to $b_{\max}\sqrt{\beta}$, where β is a uniformly distributed random variable between 0 and 1. Newton's equations of motion were integrated using a Velocity Verlet integrator with a time step of 1×10^{-16} seconds for most runs. For some 295 K translational temperature runs, a time step of 2×10^{-16} seconds was used to save computer time. Energy conservation was usually less than 0.01 kcal mol^{-1}, but was as high as 0.1 kcal mol^{-1} for some lower-temperature runs with the longer time step. The reactants were initialized 10 Å apart, and products were declared when the separation distance was greater than 10 Å. Translational temperature-dependent joint rate constants were calculated using the following equation:

$$k_n(T_t) = \left(\frac{8k_B T_t}{\pi\mu}\right)^{1/2} \overline{\sigma(n, T_t)} \tag{6}$$

where μ is the $H_2O + H_2O$ reduced mass, and $\overline{\sigma(n, T_t)}$ is the cross section averaged over the translational energy distribution function (thermally averaged cross section). The thermally averaged cross section is related to the thermally averaged probability, $P_n(T_t)$, through the following equation:

$$\overline{\sigma(n, T_t)} = \pi b_{\max}^2 P_n(T_t) \tag{7}$$

III. RESULTS

A. Vibrational Relaxation Rate Constants. Results are compared to the experiments of Zittel and Masturzo in which a laser-induced fluorescence/heated flow tube method was used.[4] After initial laser excitation of the ν_3 state, fluorescence decay as a function of time was observed in the 2.7 μm (H_2O fundamental stretch) and 6.3 μm (H_2O fundamental bend) regions. Analysis of the decay curves to yield temperature-dependent rate constants over the 295−1020 K range assumed the following kinetic scheme:[4]

Relaxation of H_2O ($\nu_2 = (010) = 1595$ cm^{-1} (4.56 kcal/mol)):

$$H_2O(\nu_2) + M \xrightarrow{k_{10}} H_2O(0) + M + 1595\ \text{cm}^{-1}\ (4.56\ \text{kcal/mol}) \tag{8}$$

Relaxation of H_2O ($2\nu_2 = (020) = 3152$ cm^{-1} (9.01 kcal/mol)):

$$H_2O(2\nu_2) + H_2O(0) \xrightarrow{k_{21}} 2H_2O(\nu_2) - 39\ \text{cm}^{-1}\ (0.11\ \text{kcal/mol}) \tag{9}$$

$$H_2O(2\nu_2) + M \xrightarrow{k'_{21}} H_2O(\nu_2) + M + 1556\ \text{cm}^{-1}\ (4.45\ \text{kcal/mol}) \tag{10}$$

$$H_2O(2\nu_2) + M \xrightarrow{k_{20}} H_2O(0) + M + 3151\ \text{cm}^{-1}\ (9.01\ \text{kcal/mol}) \tag{11}$$

Relaxation of H_2O ($\nu_3 = (001) = 3756$ cm^{-1} (10.74 kcal/mol) and $\nu_1 = (100)$ 3657 cm^{-1} (10.46 kcal/mol)):

$$H_2O(\text{stretch}) + M \xrightarrow{k_{i2}} H_2O(2\nu_2) + M + 604\ \text{cm}^{-1}\ (1.73\ \text{kcal/mol}) \tag{12}$$

$$H_2O(\text{stretch}) + H_2O(0) \xrightarrow{k_{i1}} 2H_2O(\nu_2) + 566\ \text{cm}^{-1}\ (1.62\ \text{kcal/mol}) \tag{13}$$

$$H_2O(\text{stretch}) + M \xrightarrow{k'_{i1}} H_2O(\nu_2) + M + 2161\ \text{cm}^{-1}\ (6.18\ \text{kcal/mol}) \tag{14}$$

$$H_2O(\text{stretch}) + M \xrightarrow{k_{i0}} H_2O(0) + M + 3756\ \text{cm}^{-1}\ (10.74\ \text{kcal/mol}) \tag{15}$$

$$H_2O(\nu_3) + M \overset{k_{5,4}}{\Leftrightarrow} H_2O(\nu_1) + M + 104\ \text{cm}^{-1}\ (0.30\ \text{kcal/mol}) \tag{16}$$

Here, $i = 4$ refers to the $\nu_1 = (100)$ state and $i = 5$ refers to the $\nu_3 = (001)$ state. Equilibration of the ν_1 and ν_3 states is assumed to be very fast compared to observable time scales. Analysis of the

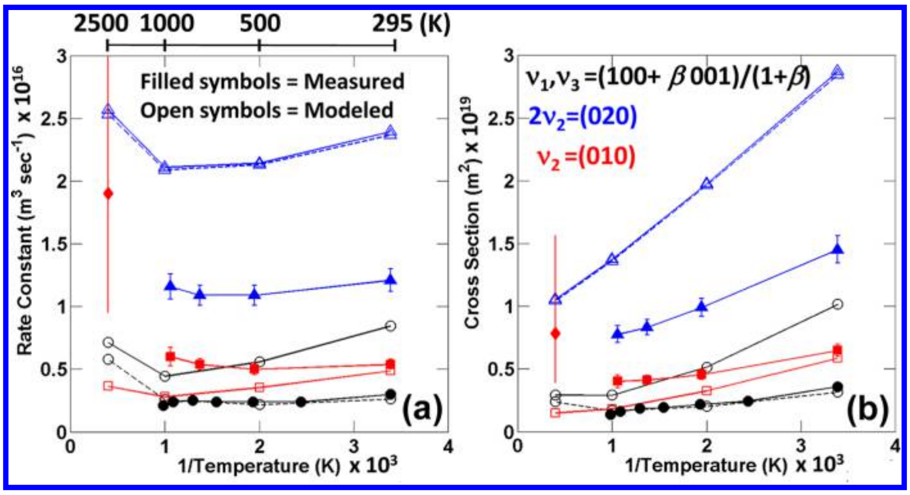

Figure 4. (a) Calculated (open symbols) and measured (filled symbols) vibrational relaxation rate constants versus $1/T$ (K). ν_1,ν_3 = (100 + β001)/(1 + β), black; ν_2 = (020), blue; and ν_2 = (010), red, where β is a temperature-dependent weighting factor. Measured results are from Zittel and Masturzo,[4] except at 2500 K which is from Kung and Center.[30] For the calculated results, the solid lines include all relaxation transitions and the dashed lines include only those transitions to the next lowest state. (b) Same as panel a except the rate constants have been divided by the velocity factor $(8k_BT/\pi\mu)^{1/2}$ to yield thermally averaged cross sections. This factor is 8.33×10^2, 1.08×10^3, 1.53×10^3, and 2.43×10^3 in units of meters per second for 295, 500, 1000, and 2500 K, respectively.

observed decay curves yielded estimates of an averaged stretch state relaxation rate constant, k_3, which is an average of the sum of all stretch state decay processes, $k_3 = (k_4 + \beta k_5)/(1 + \beta)$, where $\beta = \exp(-(104\ \text{cm}^{-1}/k_BT))$; a relaxation rate constant for the $2\nu_2$ = (020) state, k_2, which is a sum of all the $2\nu_2$ rate constants; and a relaxation rate constant for the ν_2 = (010) state, k_{10}, from 295 to 1020 K. Some bounds on the components of k_2 and k_3 were obtained. Together with other data, these bounds indicated that $H_2O(2\nu_2) + M \xrightarrow{k'_{21}} H_2O(\nu_2) + M$ was the largest component of $2\nu_2$ relaxation and $H_2O(\text{stretch}) + M \xrightarrow{k_{32}} H_2O(2\nu_2) + M$ was the largest component of the stretch relaxation.

Implicit in writing the above kinetic equations is that unless otherwise noted the collision partner M is the vibrational ground state of H_2O, and except for k_{21} and k_{i1} processes, M does not change its vibrational state. In fact, the measurements cannot distinguish between the initially excited $H_2O(1)$ and its collision partner, and contributions from both will contribute to the rate constant.[29] For example, the rate constant k'_{21} is a sum of contributions from two processes:

$$H_2O(1, \nu = (020)) + H_2O(2, \nu = (000)) \rightarrow H_2O(1, \nu = (010)) + H_2O(2, \nu = (000)) \tag{17}$$

and

$$H_2O(1, \nu = (020)) + H_2O(2, \nu = (000)) \rightarrow H_2O(1, \nu = (000)) + H_2O(2, \nu = (010)) \tag{18}$$

The present calculations, which distinguish between these two processes, therefore sum these contributions for comparison to the measurements. We note also that the energy defects listed in the kinetic scheme, for illustrative purposes, assume the stretch is (001).

Figure 4a shows the experimental rate constant measurements of Zittel and Masturzo from 295 to 1020 K (ref 4) and a single data point at 2500 K for the fundamental bending relaxation, ν_2 = (010), from ref 30. All experimental results are shown with solid lines and filled symbols. Figure 4a also shows the present calculated vibrational relaxation rate constants as solid and dashed lines with open symbols. The calculated results for ν_3 and ν_1 are combined into a weighted average stretch relaxation rate constant, $k_3 = (k_4 + \beta k_5)/(1 + \beta)$, where $\beta = \exp(-(104\ \text{cm}^{-1}/k_BT))$, to compare directly with the experimental results. The statistical uncertainty of the calculated results varies from less than 10% for the stretch results to less than 2% for the $2\nu_2$ results. The uncertainty was estimated by dividing all trajectories into five batches, calculating rate constants separately for each batch, and then estimating the standard deviation from this five-sample set. The calculated result solid lines were obtained by summing all rate constants for processes which result in a lower vibrational state than the initially vibrationally excited water. Therefore, the solid line calculated stretch rate constant includes all processes in which both product waters are in the $2\nu_2$, ν_2, or ground state. The solid line calculated $2\nu_2$ rate constant includes all processes in which both product waters are in the ν_2 or the ground state. The solid line ν_2 rate constant includes the single process in which both product waters are in the ground vibrational state. Rate constants calculated in this way should be most comparable with the experimentally reported rate constants.

To indicate the relative importance of particular vibrational final states, the dashed lines of Figure 4a give the calculated rate constants obtained by including only those processes in which product waters go to the next lowest vibrational state (for the stretch relaxation, only stretch $\rightarrow 2\nu_2$, and for $2\nu_2$ relaxation, only $2\nu_2 \rightarrow \nu_2$). This makes a large difference in the stretch states at lower temperatures, where the dominant rate is the $H_2O(\text{stretch}) \rightarrow H_2O(\nu_2)$ process. The present results are generally about a factor of 2 larger than the results of Zittel and Masturzo,[4] with the best agreement for ν_2 relaxation at low temperature. The present calculated results assume that the $H_2O(1)$ initially excited water has no rotational energy. In fact, the $H_2O(1)$ may be wholly or partly equilibrated in the measurements below 1000 K. Inclusion of this rotational energy would probably tend to increase the calculated rate constant to some extent, making the overall agreement somewhat worse.

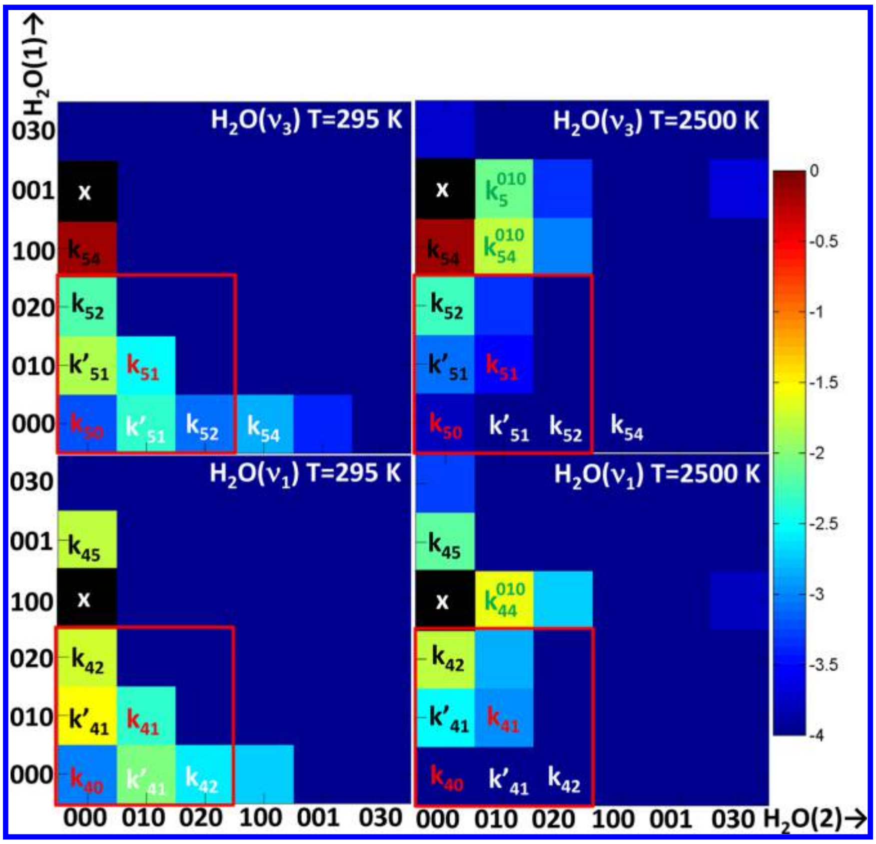

Figure 5. Thermally averaged joint probabilities to $H_2O(1,\nu)$ + $H_2O(2,\nu)$ for initially excited ν_3 and ν_1 states of $H_2O(1)$ at 295 and 2500 K. A log10 scale is used, and each matrix has been normalized to sum to 1.0.

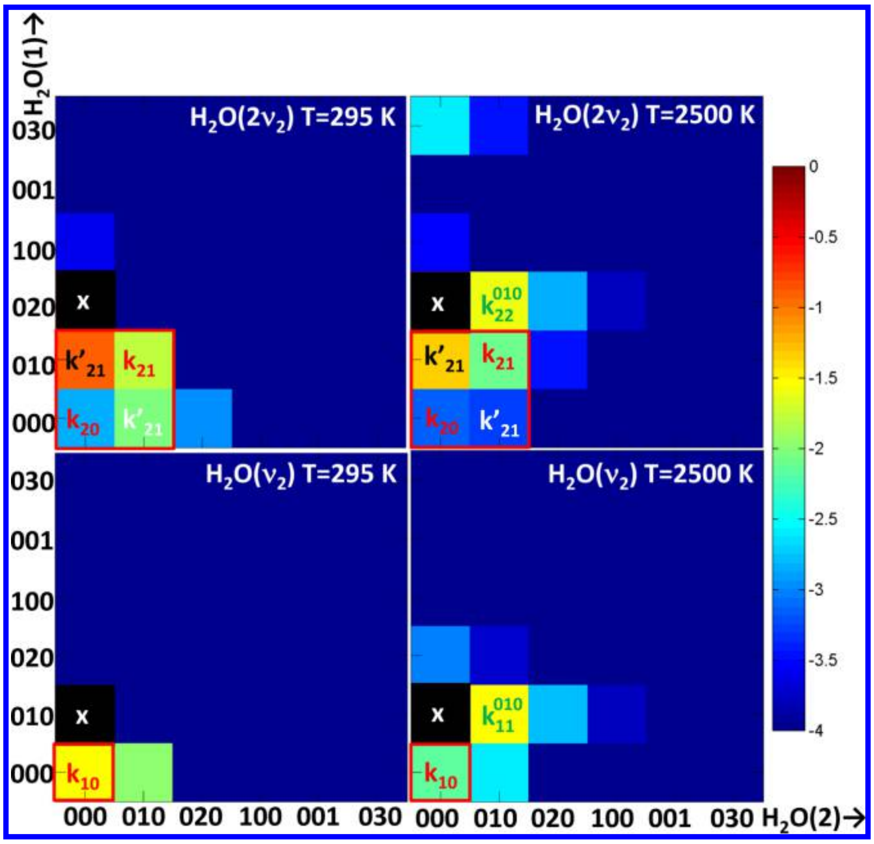

Figure 6. Thermally averaged joint probabilities to $H_2O(1,\nu)$ + $H_2O(2,\nu)$ for initially excited $2\nu_2$ and ν_2 states of $H_2O(1)$ at 295 and 2500 K. A log10 scale is used, and each matrix has been normalized to sum to 1.0.

Table 2. Thermally Averaged Joint Probabilities for $H_2O(1,\nu)$ + $H_2O(2,\nu)$ Corresponding to Figures 5 and 6

	$H_2O(2)$ 000	$H_2O(2)$ 010	$H_2O(2)$ 020	$H_2O(2)$ 100	$H_2O(2)$ 001	$H_2O(2)$ 030
(a) ν_3 = (001) of $H_2O(1)$ at 295 K						
$H_2O(1)$ 000	6.03×10^{-4}	4.36×10^{-3}	8.28×10^{-4}	1.48×10^{-3}	4.16×10^{-4}	0.00×10^{0}
$H_2O(1)$ 010	1.34×10^{-2}	2.81×10^{-3}	0.00×10^{0}	0.00×10^{0}	0.00×10^{0}	0.00×10^{0}
$H_2O(1)$ 020	5.75×10^{-3}	0.00×10^{0}	0.00×10^{0}	0.00×10^{0}	0.00×10^{0}	0.00×10^{0}
$H_2O(1)$ 100	6.50×10^{-1}	0.00×10^{0}	0.00×10^{0}	0.00×10^{0}	0.00×10^{0}	0.00×10^{0}
$H_2O(1)$ 001	X	0.00×10^{0}	0.00×10^{0}	0.00×10^{0}	0.00×10^{0}	0.00×10^{0}
$H_2O(1)$ 030	0.00×10^{0}	0.00×10^{0}	0.00×10^{0}	0.00×10^{0}	0.00×10^{0}	0.00×10^{0}
(b) ν_3 = (001) of $H_2O(1)$ at 2500 K						
$H_2O(1)$ 000	1.75×10^{-4}	1.15×10^{-4}	0.00×10^{0}	0.00×10^{0}	0.00×10^{0}	0.00×10^{0}
$H_2O(1)$ 010	8.01×10^{-4}	3.10×10^{-4}	0.00×10^{0}	0.00×10^{0}	0.00×10^{0}	0.00×10^{0}
$H_2O(1)$ 020	5.31×10^{-3}	4.65×10^{-4}	0.00×10^{0}	0.00×10^{0}	0.00×10^{0}	0.00×10^{0}
$H_2O(1)$ 100	6.53×10^{-1}	1.74×10^{-2}	9.60×10^{-4}	0.00×10^{0}	0.00×10^{0}	1.11×10^{-4}
$H_2O(1)$ 001	X	8.58×10^{-3}	4.65×10^{-4}	0.00×10^{0}	0.00×10^{0}	2.10×10^{-4}
$H_2O(1)$ 030	1.79×10^{-4}	0.00×10^{0}	0.00×10^{0}	0.00×10^{0}	0.00×10^{0}	0.00×10^{0}
(c) ν_1 = (100) of $H_2O(1)$ at 295 K						
$H_2O(1)$ 000	9.56×10^{-4}	8.69×10^{-3}	2.64×10^{-3}	1.82×10^{-3}	1.01×10^{-4}	0.00×10^{0}
$H_2O(1)$ 010	2.88×10^{-2}	4.72×10^{-3}	0.00×10^{0}	0.00×10^{0}	0.00×10^{0}	0.00×10^{0}
$H_2O(1)$ 020	1.85×10^{-2}	0.00×10^{0}	0.00×10^{0}	0.00×10^{0}	0.00×10^{0}	0.00×10^{0}
$H_2O(1)$ 100	X	0.00×10^{0}	0.00×10^{0}	0.00×10^{0}	0.00×10^{0}	0.00×10^{0}
$H_2O(1)$ 001	1.69×10^{-2}	0.00×10^{0}	0.00×10^{0}	0.00×10^{0}	0.00×10^{0}	0.00×10^{0}
$H_2O(1)$ 030	0.00×10^{0}	0.00×10^{0}	0.00×10^{0}	0.00×10^{0}	0.00×10^{0}	0.00×10^{0}
(d) ν_1 = (100) of $H_2O(1)$ at 2500 K						
$H_2O(1)$ 000	0.00×10^{0}	0.00×10^{0}	0.00×10^{0}	0.00×10^{0}	0.00×10^{0}	0.00×10^{0}
$H_2O(1)$ 010	2.90×10^{-3}	1.01×10^{-3}	0.00×10^{0}	0.00×10^{0}	0.00×10^{0}	0.00×10^{0}
$H_2O(1)$ 020	1.61×10^{-2}	1.40×10^{-3}	0.00×10^{0}	0.00×10^{0}	0.00×10^{0}	0.00×10^{0}
$H_2O(1)$ 100	X	2.67×10^{-2}	1.93×10^{-3}	0.00×10^{0}	0.00×10^{0}	1.70×10^{-4}
$H_2O(1)$ 001	7.25×10^{-3}	0.00×10^{0}	0.00×10^{0}	0.00×10^{0}	0.00×10^{0}	0.00×10^{0}
$H_2O(1)$ 030	4.93×10^{-4}	0.00×10^{0}	0.00×10^{0}	0.00×10^{0}	0.00×10^{0}	0.00×10^{0}
(e) $2\nu_2$ = (020) of $H_2O(1)$ at 295 K						
$H_2O(1)$ 000	1.49×10^{-3}	9.38×10^{-3}	1.10×10^{-3}	0.00×10^{0}	0.00×10^{0}	0.00×10^{0}
$H_2O(1)$ 010	1.16×10^{-1}	1.58×10^{-2}	0.00×10^{0}	0.00×10^{0}	0.00×10^{0}	0.00×10^{0}
$H_2O(1)$ 020	X	0.00×10^{0}	0.00×10^{0}	0.00×10^{0}	0.00×10^{0}	0.00×10^{0}
$H_2O(1)$ 100	2.63×10^{-4}	0.00×10^{0}	0.00×10^{0}	0.00×10^{0}	0.00×10^{0}	0.00×10^{0}
$H_2O(1)$ 001	0.00×10^{0}	0.00×10^{0}	0.00×10^{0}	0.00×10^{0}	0.00×10^{0}	0.00×10^{0}
$H_2O(1)$ 030	0.00×10^{0}	0.00×10^{0}	0.00×10^{0}	0.00×10^{0}	0.00×10^{0}	0.00×10^{0}
(f) $2\nu_2$ = (020) of $H_2O(1)$ at 2500 K						
$H_2O(1)$ 000	6.94×10^{-4}	5.05×10^{-4}	0.00×10^{0}	0.00×10^{0}	0.00×10^{0}	0.00×10^{0}
$H_2O(1)$ 010	4.37×10^{-2}	7.73×10^{-3}	3.29×10^{-4}	0.00×10^{0}	0.00×10^{0}	0.00×10^{0}
$H_2O(1)$ 020	X	2.73×10^{-2}	1.49×10^{-3}	1.68×10^{-4}	0.00×10^{0}	0.00×10^{0}
$H_2O(1)$ 100	2.85×10^{-4}	0.00×10^{0}	0.00×10^{0}	0.00×10^{0}	0.00×10^{0}	0.00×10^{0}
$H_2O(1)$ 001	0.00×10^{0}	0.00×10^{0}	0.00×10^{0}	0.00×10^{0}	0.00×10^{0}	0.00×10^{0}
$H_2O(1)$ 030	2.51×10^{-3}	3.63×10^{-4}	0.00×10^{0}	0.00×10^{0}	0.00×10^{0}	0.00×10^{0}
(g) ν_2 = (010) of $H_2O(1)$ at 295 K						
$H_2O(1)$ 000	2.92×10^{-2}	1.08×10^{-2}	0.00×10^{0}	0.00×10^{0}	0.00×10^{0}	0.00×10^{0}
$H_2O(1)$ 010	X	0.00×10^{0}	0.00×10^{0}	0.00×10^{0}	0.00×10^{0}	0.00×10^{0}
$H_2O(1)$ 020	0.00×10^{0}	0.00×10^{0}	0.00×10^{0}	0.00×10^{0}	0.00×10^{0}	0.00×10^{0}
$H_2O(1)$ 100	0.00×10^{0}	0.00×10^{0}	0.00×10^{0}	0.00×10^{0}	0.00×10^{0}	0.00×10^{0}
$H_2O(1)$ 001	0.00×10^{0}	0.00×10^{0}	0.00×10^{0}	0.00×10^{0}	0.00×10^{0}	0.00×10^{0}
$H_2O(1)$ 030	0.00×10^{0}	0.00×10^{0}	0.00×10^{0}	0.00×10^{0}	0.00×10^{0}	0.00×10^{0}
(h) ν_2 = (010) of $H_2O(1)$ at 2500 K						
$H_2O(1)$ 000	7.47×10^{-3}	2.47×10^{-3}	0.00×10^{0}	0.00×10^{0}	0.00×10^{0}	0.00×10^{0}
$H_2O(1)$ 010	X	2.91×10^{-2}	1.75×10^{-3}	1.67×10^{-4}	0.00×10^{0}	1.01×10^{-4}
$H_2O(1)$ 020	9.03×10^{-4}	1.96×10^{-4}	0.00×10^{0}	0.00×10^{0}	0.00×10^{0}	0.00×10^{0}
$H_2O(1)$ 100	0.00×10^{0}	0.00×10^{0}	0.00×10^{0}	0.00×10^{0}	0.00×10^{0}	0.00×10^{0}
$H_2O(1)$ 001	0.00×10^{0}	0.00×10^{0}	0.00×10^{0}	0.00×10^{0}	0.00×10^{0}	0.00×10^{0}
$H_2O(1)$ 030	0.00×10^{0}	0.00×10^{0}	0.00×10^{0}	0.00×10^{0}	0.00×10^{0}	0.00×10^{0}

The present results are about a factor of 4 lower than the measurement of Kung et al. at 2500 K, although the experimental error bars are relatively large.[30] The lower edge of the experimental uncertainty is within a factor of ~2 of the calculated result. Inclusion of rotational energy in the $H_2O(1)$ initially excited molecule at 2500 K would likely increase the

Table 3. Rate Constant Component Ratios versus Temperature

	measurement bounds of Zittel and Masturzo[4]			present calculated results			
	T = 295 K	T = 514 K	T = 947 K	T = 295 K	T = 500 K	T = 1000 K	T = 2500 K
k_{21}/k_2	≤0.54	≤0.50	≤0.44	0.11	0.14	0.14	0.15
k'_{21}/k_2	≥0.31	≥0.33	≥0.33	0.88	0.86	0.85	0.84
k_{32}/k_3	≥0.32	≥0.33	≥0.35	0.31	0.39	0.58	0.74

calculated results significantly and may account for most of this difference. We have attempted trajectory calculations which include the $H_2O(1)$ rotational energy at 2500 K. However, the convergence with impact parameter for these "large target" trajectories became problematic and could not be completed.

The rate constant values either level off or increase as the temperature decreases, which is opposite to expectations from well-known vibrational relaxation theories.[7] Figure 4b shows the same data as Figure 4a, except the rate constants have been divided by the temperature factor $(8k_BT/\pi\mu)^{1/2}$ to yield thermally averaged cross sections, $\overline{\sigma(n,\ T_t)}$. These cross sections show more dramatically an increase with decreasing temperature. Examination of the calculated translational energy dependence of the relaxation cross sections shows either a flat behavior with collision energy or an increase with decreasing collision energy. This behavior at low collision energy is different than that usually assumed by simple models of vibrational relaxation and is closer to the behavior of low or zero activation energy chemical reactions with potential wells. We have not further reduced these thermally averaged cross sections to probabilities by dividing by an area because we have found that the usual single-value van-der-Waals radius used for the area does not apply. In fact, we have found that the range of important impact parameters extends to 8 Å, much larger than the 2.8 Å used in Zittel and Masturzo.[4] Using the radius value of 2.8 Å results in some relaxation probabilities larger than 1.0.

Besides the total relaxation rate constants and thermally averaged cross sections from particular vibrational states discussed above, the present calculations also yield "joint" vibrational rate constants and cross sections where both water product states ($H_2O(1,\nu) + H_2O(2,\nu)$) are specified. Figures 5 and 6 show the thermally averaged joint probabilities, normalized to sum to 1.0, for the processes $H_2O(1,\nu = \nu_2, 2\nu_2, \nu_1, \nu_3) + H_2O(2,\nu = 0)$ at 295 K and 2500 K. Each matrix element in Figures 5 and 6 corresponds to a vibrationally state specific joint product probability. The matrix elements are ordered by increasing energy. These probabilities will depend on the value of b_{max} used in the present simulations and do not correspond to "relaxation probabilities" as normally understood. These "intermediate" probabilities, however, can be converted to thermally averaged joint cross sections by multiplying by πb_{max}^2, where in the present calculations $b_{max} = 8 \times 10^{-10}$ m. Likewise, the joint probabilities can be converted to joint thermal rate constants by multiplying by the factor, $\pi b_{max}^2(8k_BT/\pi\mu)^{1/2}$. For rate constant units of cubic meters per second, these values are 1.68×10^{-15}, 2.17×10^{-15}, 3.08×10^{-15}, and 4.89×10^{-15} for 295, 500, 1000, and 2500 K, respectively. Some matrix elements in Figures 5 and 6 have been labeled according to their identity in the kinetic rate equations of Zittel and Masturzo,[4] as presented above. The diagonal elements in Figures 5 and 6 are color coded in red and correspond to processes in which both water products are in the same vibrational state. The black color code corresponds to $H_2O(2)$ staying in the ground state. The white color code corresponds to the product $H_2O(1)$ going to the ground state, where the product $H_2O(1)$ and $H_2O(2)$ are swapped from the corresponding black color code process. All processes with products in the red boxes are counted toward the total relaxation processes when comparing to measurements. The label "X" corresponds to vibrationally elastic transitions which cannot be properly captured in the present classical calculations and should be ignored. The color scheme is on a log10 scale for clarity. We also note that there are several more transitions possible than in the basic kinetic scheme used in the original measurement analysis. For completeness, the numerical values of the thermally averaged joint probabilities corresponding to Figures 5 and 6 are given in parts a–h of Table 2, where values less than 1.0×10^{-4} have been set to zero because of their relatively large statistical uncertainty.

As pointed out earlier, the calculations show that stretching relaxation at lower temperatures favors relaxation to $H_2O(1,\nu = (010))$ rather than $H_2O(1,\ \nu = (020))$. Furthermore, it is clear that significant vibrational excitation of the $H_2O(2)$ partner can occur. For example, at lower temperatures, initial $H_2O(1)$ stretching excitation can lead to excitation of the $H_2O(2)$ vibrational states. For initial $H_2O(1)$ ν_2 and $2\nu_2$ vibration, relaxation at low temperatures can also lead to excitation of $H_2O(2)$ bending vibration. In Figure 5, it is also clear that the $\nu_1 = (100)$ relaxation rate constants are generally significantly larger than the $\nu_3 = (001)$ relaxation rate constants.

We should also point out that at 2500 K, there are significant processes which correspond to excitation rather than relaxation. These are color coded in green (for example, k_{11}^{010} in Figure 6) and mostly involve excitation of the $H_2O(2,\ \nu = (010))$ state. The calculated excitation processes can be larger than relaxation processes and may complicate the interpretation of measurements in this temperature range. On the other hand, from detailed balance arguments, one may expect that, for example, k_{11}^{010} should be smaller than the relaxation process rate constant k_{10}.

$$k_{10}\!:\ H_2O(1,\ \nu = (010)) + H_2O(2,\ \nu = (000)) \rightarrow H_2O(1,\ \nu = (000)) + H_2O(2,\ \nu = (000)) \qquad (19)$$

and

$$k_{11}^{010}\!:\ H_2O(1,\ \nu = (010)) + H_2O(2,\ \nu = (000)) \rightarrow H_2O(1,\ \nu = (010)) + H_2O(2,\ \nu = (010)) \qquad (20)$$

However, for these processes, especially k_{11}^{010}, we have found that the product waters are highly nonthermal, and detailed balance arguments cannot be applied.

Table 3 shows the experimentally derived bounds from Zittel and Masturzo[4] for some state-specific rate constants expressed as ratios to the total vibrational relaxation rate constant. The left-hand part of Table 3 shows the experimental results. The right-hand part of Table 3 shows the corresponding calculated quantities. The calculated ratios are in agreement with the measured bounds, except for (k_{32}/k_3) at 295 K, which is slightly

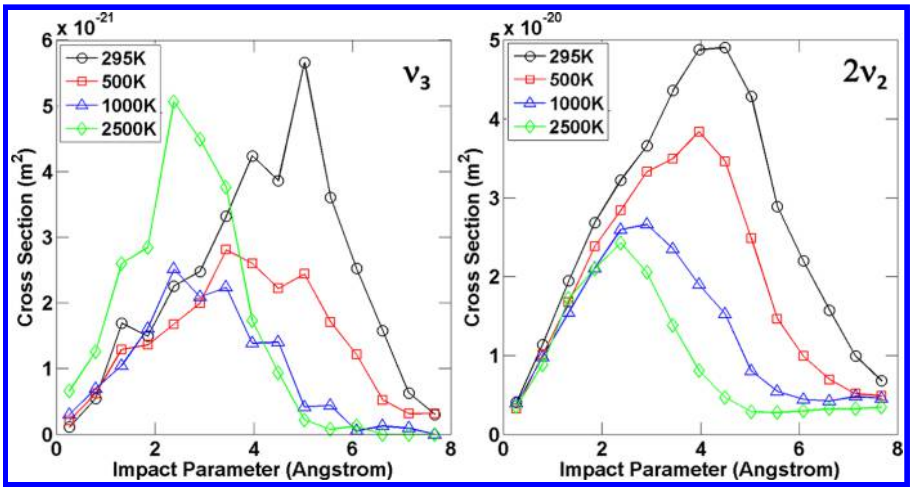

Figure 7. Thermally averaged cross sections, $\overline{\Delta\sigma_n(b_i,\ T_t)}$, versus impact parameter bin, b_i, for initially excited ν_3 and $2\nu_2$ states of H_2O leading to relaxation of $H_2O(1)$ at 295, 500, 1000, and 2500 K.

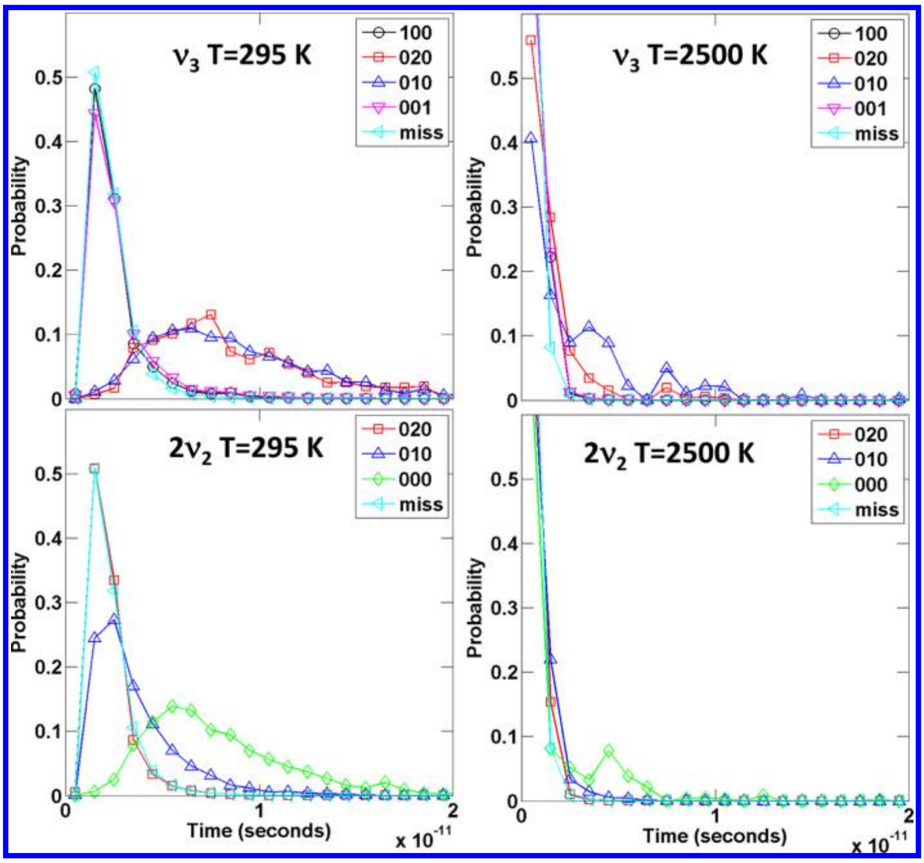

Figure 8. Normalized probability distribution function versus trajectory time for initially excited ν_3 and $2\nu_2$ states of H_2O at 295 and 2500 K. Each color is for relaxation to a different $H_2O(1)$ vibrational final state, and "miss" corresponds to an initial Boltzmann translational distribution and no interaction.

lower than the measured value. In the calculated results at low temperature, the stretch to ν_2 state, with a larger vibrational energy change, is the largest contributor. This is consistent with the fairly loose bounds provided by the measurement ratios.

B. Vibrational Self-Relaxation Mechanisms. To help understand the mechanism of vibrational relaxation, Figure 7 shows the thermally averaged cross section versus impact parameter for relaxation of $H_2O(1,\nu_3 = (001))$ to $H_2O(1,2\nu_2 = (020))$ and $H_2O(1,2\nu_2 = (020))$ to $H_2O(1,\nu_2 = (010))$ at all the temperatures studied. The thermally averaged cross section at a particular impact parameter bin, b_i, is defined as

$$\overline{\Delta\sigma_n(b_i,\ T_t)} = \frac{2\pi G_n(b_i,\ T_t) b_i \Delta b_i}{G_{tot}(b_i,\ T_t)} \tag{21}$$

where i denotes an impact parameter bin; $G_n(b_i,\ T_t)$ is the Gaussian weight for the joint vibrational product states $n = \{H_2O(1,\nu) + H_2O(2,\nu)\}$ in impact parameter bin b_i, and $G_{tot}(b_i,\ T_t)$ is the sum of $G_n(b_i,\ T_t)$ over all joint product states, n. Figure

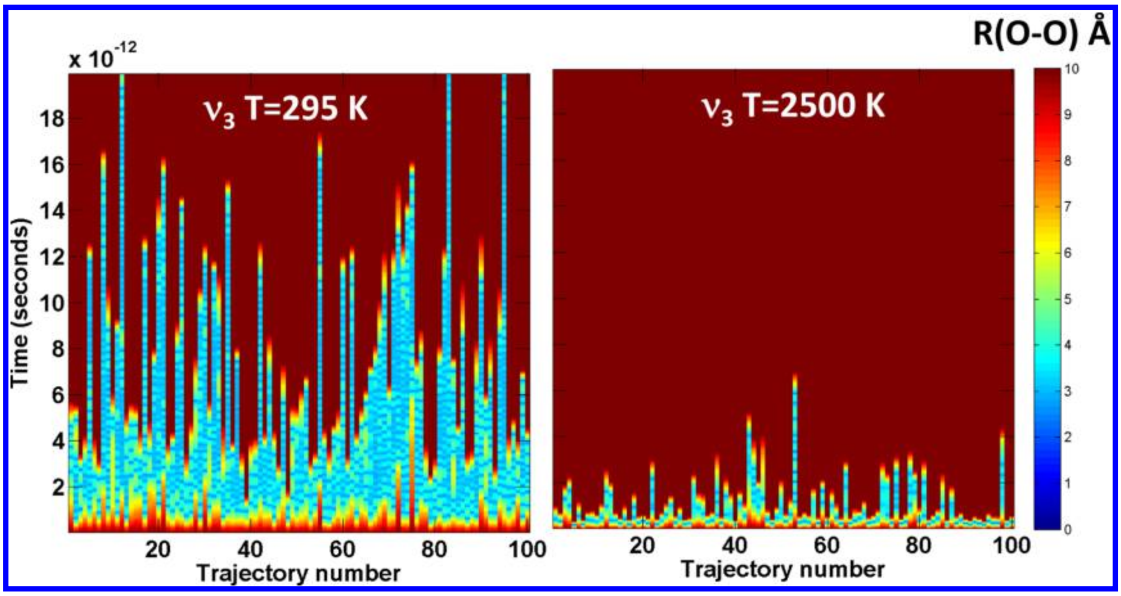

Figure 9. Oxygen−oxygen distance of 100 representative trajectories for initially excited ν_3 leading to vibrational relaxation at 295 and 2500 K.

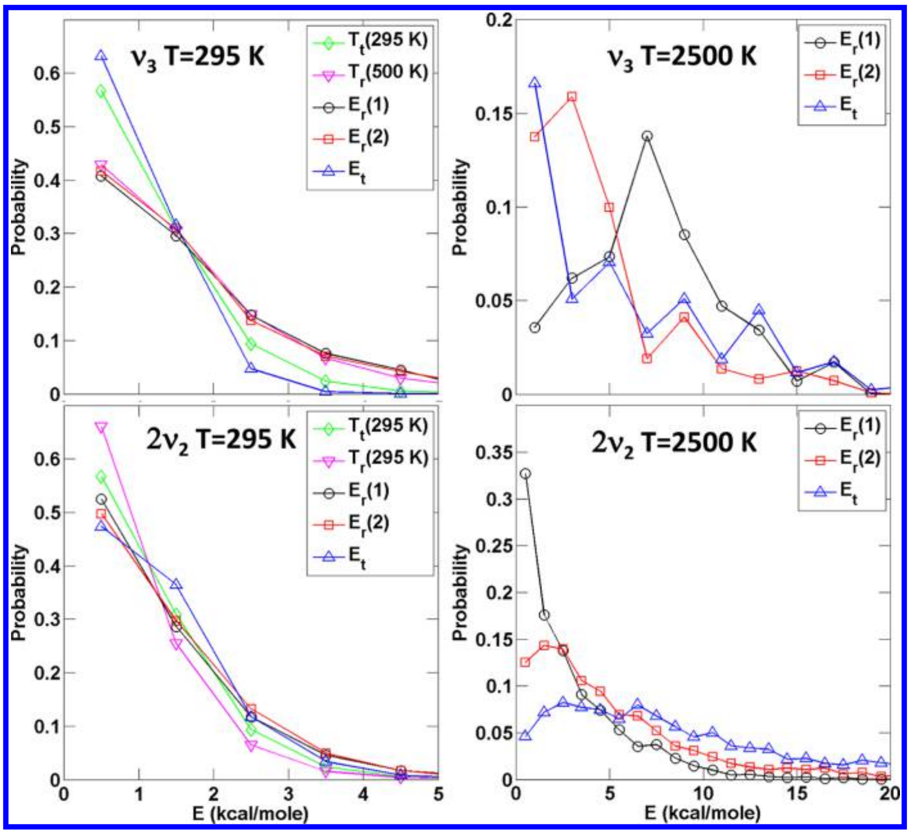

Figure 10. Final state rotational distributions, $E_r(1)$ for $H_2O(1)$ and $E_r(2)$ for $H_2O(2)$, and final translational energy distributions, E_t, between the two water products for ν_3 and $2\nu_2$ relaxation of initially excited $H_2O(1)$ at 295 and 2500 K. At 295 K, also shown are Boltzmann rotational, T_r, and translational, T_t, distributions, as purple and green lines, respectively, for comparison.

7 shows that the largest contribution to the rate constant at temperatures above 1000 K is centered near 2.5 Å, but it then shifts with decreasing temperature to 5 Å at 295 K. At 295 K, contributions up to 8 Å are important.

Shin pointed out that the mechanism for H_2O vibrational self-relaxation involves long-lived trajectories.[9] By examination of individual trajectories we have found this to be the case in the present calculations as well, at least at low temperatures. At low temperatures, trajectories leading to relaxation can form a complex in which the two waters oscillate against each other for several vibrational periods, as if connected by a large and loose rubber band. To put this on a more quantitative basis, Figure 8 shows the normalized probability distribution functions versus the classical trajectory time for relaxation of ν_3 and $2\nu_2$ broken down into final $H_2O(1)$ states at 295 and 2500 K. The classical trajectory time is defined as the time taken from the start of the trajectory when the two waters are 10 Å apart to when water products are separated by 10 Å at the end of a trajectory. We also plot the "miss" mode probability. The miss mode probability is analytic. The miss mode probability versus time is defined as 20 Å divided by the speed distribution corresponding to a given translational temperature. This miss mode corresponds to no interaction and strongly overlaps with the elastic, nonvibrational changing transition results. At 295 K, $\nu_3 \rightarrow 2\nu_2$, $\nu_3 \rightarrow \nu_2$, and the $2\nu_2 \rightarrow (000)$ processes have broad probability distribution functions versus time, peaked around 7.0×10^{-12} seconds, which are near values found by Shin. At 2500 K, these long-time peaks shift to shorter times and become far less important. Furthermore, the long-time tails are mostly gone. For higher temperatures, most of the relaxation transitions occur for trajectory times which are the same as the miss trajectory times.

To examine the trajectories further, the distance between the oxygen atoms versus time for 100 randomly chosen trajectories at 295 and 2500 K which lead to ν_3 relaxation are shown in Figure 9. The color wash indicates the oxygen−oxygen distance in angstroms. Red indicates far distances at the beginning and ending of a trajectory. The banded blue-green alternating structure within a single trajectory indicates oscillation of the oxygen atoms between ∼3 Å and ∼5 Å. Several of the 295 K trajectories show more than 50 of these oscillations in 2.0×10^{-11} seconds. For reference, low-lying periodic vibrational and rotational motions in isolated H_2O are on the order of 1.0×10^{-14} and 1.0×10^{-12} seconds, respectively. At 2500 K, many of the trajectories show no oscillation, while the longest-lived complexes oscillate about 10 times. Rate constants are still fairly large at 2500 K, even without many long-lived collision complexes.

Figure 10 shows the calculated product rotational and translational energy probability distribution functions for relaxation of the ν_3 and $2\nu_2$ states at 295 and 2500 K. Each distribution is normalized to integrate to 1.0. For the $2\nu_2$ state at 295 K, the rotational distribution of both H_2O products, $E_r(1)$ and $E_r(2)$, and the product relative translational energy distribution are all nearly identical to each other. They are also well fit by their respective Boltzmann translational and rotational distributions at 295 K which are also shown in the figure for reference. The similarity of both water product rotational distributions to each other was also seen in the vibrational predissociation study of Ch'ng et al., in which the product donor and acceptor waters had nearly the same angular momentum distributions.[10] The rotational mode of the initially vibrationally excited $H_2O(1)$, which started with a rotational energy of zero, has fully "equilibrated" with the rotational motion of its collision partner, $H_2O(2)$, during the long lifetime of the collision complex formed at these low temperatures. The vibrational energy lost by $H_2O(1)$ has been partly regained in its rotational mode. The translational energy distribution is nearly unchanged in the collision, which suggests translation has a small role in the dynamics. For the ν_3 state at 295 K, the rotational distributions of the two waters are also still nearly identical, but now are well represented by a Boltzmann temperature of 500 K. The translational energy distribution is correspondingly slightly colder than 295 K.

At 2500 K, none of the distributions fit a single temperature well, but all have long energy tails. For the $2\nu_2$ state, the rotational energy distributions above 5 kcal mol^{-1} of both waters are similar to each other and are close to H_2O rotational distributions of ∼1000 K. The translational energy distribution above 5 kcal mol^{-1} is similar to the rotational distributions and resembles the 2500 K Boltzmann translational energy distributions. For ν_3 at 2500 K, there is much statistical scatter, but it is clear the distributions also have long energy tails. It is also clear that the rotational distributions of the two waters are different. The initially vibrationally excited water $H_2O(1)$ has a peak near 7 kcal mol^{-1}, and the partner $H_2O(2)$ has a low-energy peak and high-energy tail. The initially vibrationally excited water, $H_2O(1)$, which initially had no rotational energy, has taken away rotational energy from its collision partner. For these high-temperature distributions, there is much less "equilibration" of the energy modes than at lower temperatures. This is likely due to the interaction not going through a long-lived collision complex as seen at low temperatures.

IV. CONCLUSIONS

The present vibrational self-relaxation simulations examine long-lived complexes, rate constant increases with decreasing temperature, and the participation of energy modes of the molecular partner. Similar behavior has been observed in other hydrogen bonded systems[8] and in the relaxation of CH radical with N_2 and CO.[11] The present study shows the importance of large impact parameters, out to 8 Å, to treat the lowest temperatures studied here. Although long-lived (compared to vibrational and rotational motion of single H_2O) collision complexes up to 20 ps were clearly important for lower temperatures, they were not necessary to produce the still fairly large rate constant values at the higher temperatures (>1000 K). At low temperatures, the rotational mode of the initially vibrationally excited H_2O which started with a rotational energy of zero, fully "equilibrates" with the initial rotational energy distribution of its collision partner. The translational energy distribution is nearly unchanged at low temperature for vibrational relaxation. The equal sharing of rotational energy was also seen in the vibrational predissociation studies of the water dimer of Ch'ng et al.[10] Ch'ng et al. also found long-lived interactions, dominant stretch-to-bend pathways, and the participation of both the initially excited and partner H_2O molecules, consistent with the vibrational relaxation dynamics observed here.

At higher temperatures there are few long-lived complexes. The rotational mode of the relaxing H_2O takes away substantial rotational energy from its collision partner, leaving two distinct rotational distributions which are not well characterized by a single temperature. Although the vibrational relaxation rate constants remain large at high temperature, there is a transition of the underlying mechanism of interaction and energy distribution in the products which occurs around 500−1000 K.

The present calculations confirm the importance of the stretch-to-bend pathway for vibrational relaxation. At 295 K, the dominant channel was found to be stretch to one quantum of bend. This finding is consistent with the measured bounds of the component rate constants[4] but disagrees with previous interpretations of the measured data,[4,9] which ascribes the major relaxation pathway to the stretch-to-two quantum bend channel. The present calculations suggest that the dominant channel changes from stretch-one-quantum-bend to stretch-two-quantum-bend with increasing temperature.

The present classically based rate constants do not take into account several effects which may be potentially important: quantum tunneling, the guarantee of microscopic reversibility,[31] or the mixing of initial vibrationally excited states. Nevertheless, the calculated results are generally within a factor of 2 or better of the measured vibrational relaxation rate constant values. The present H_2O + H_2O surface and classical dynamics approach is therefore well-suited to analyze the measurements of the fast H_2O self-relaxation combination $\nu_1 + \nu_2$ and $\nu_3 + \nu_2$ states[32] and of the excited $(|04\rangle^-)$ state.[33] The present approach also gives joint molecule-specific vibrational rate constants, which can be used to guide future highly detailed measurements of this fundamental system. The present study may also provide insight into the vibrational relaxation of liquid water, which is of central importance in condensed phase reactive chemistry.[34] Finally, it is hoped that the present study will point the way toward a simple, predictive model, such as that reported in ref 7, which has been so successful for other molecular systems.

■ AUTHOR INFORMATION

Corresponding Author

*Email: matthew.braunstein@spectral.com.

Notes

The authors declare no competing financial interest.

■ ACKNOWLEDGMENTS

The authors gratefully acknowledge the use of the potential surface fitting programs of B. J. Braams and J. Bowman. P. Zittel, I. Wysong, R. Dressler, and T. Deschenes provided extremely helpful comments on initial drafts.

■ REFERENCES

(1) Tschumper, G. S.; Leininger, M. L.; Hoffman, B. C.; Valeev, E. F.; Schaefer, H. F.; Quack, M. Anchoring the Water Dimer Potential Energy Surface with Explicitly Correlated Computations and Focal Point Analyses. *J. Chem. Phys.* **2002**, *116*, 690−701.

(2) Tretyakov, M.; Serov, E.; Koshelev, M.; Parshin, V.; Krupnov, A. Water Dimer Rotationally Resolved Millimeter-Wave Spectrum Observation at Room Temperature. *Phys. Rev. Lett.* **2013**, *110*, 093001.

(3) Finzi, J.; Hovis, F. E.; Panfilov, V. N.; Hess, P.; Moore, C. B. Vibrational Relaxation of Water Vapor. *J. Chem. Phys.* **1977**, *67*, 4053−4061.

(4) Zittel, P. F.; Masturzo, D. E. Vibrational Relaxation of H_2O from 295 to 1021 K. *J. Chem. Phys.* **1989**, *90*, 977−989.

(5) Landau, L.; Teller, E. Theory of Monomolecular Reactions. *Phys. Z. Sowjetunion* **1936**, *10*, 34.

(6) Parker, J. G. Rotational and Vibrational Relaxation in Diatomic Gases. *Phys. Fluids* **1959**, *2*, 449−462.

(7) Millikan, R. C.; White, D. R. Systematics of Vibrational Relaxation. *J. Chem. Phys.* **1963**, *39*, 3209−3213.

(8) Zittel, P. F.; Moore, C. B. Vibrational Relaxation in HBr and HCl from 144°K to 584°K. *J. Chem. Phys.* **1973**, *59*, 6636−6640.

(9) Shin, H. K. Self-Relaxation of Vibrationally Excited H_2O Molecules. *J. Chem. Phys.* **1993**, *98*, 1964−1978.

(10) Ch'ng, L. C.; Samanta, A. K.; Czakó, G.; Bowman, J. M.; Reisler, H. Experimental and Theoretical Investigations of Energy Transfer and Hydrogen-Bond Breaking in the Water Dimer. *J. Am. Chem. Soc.* **2012**, *134*, 15430−15435.

(11) Herbert, L. B.; Sims, I. R.; Smith, I. W. M.; Stewart, D. W. A.; Symonds, A. C.; Canosa, A.; Rowe, B. R. Rate Constants for the Relaxation of $CH(X^2\Pi,\nu=1)$ by CO and N_2 at Temperatures from 23 to 584 K. *J. Phys. Chem.* **1996**, *100*, 14928−14935.

(12) Frisch, M. J.; Trucks, G. W.; Schlegel, H. B.; Scuseria, G. E.; Robb, M. A.; Cheeseman, J. R.; Montgomery, J. A., Jr., et al. *Gaussian 03*, revision C.02; Gaussian, Inc.: Wallingford, CT, 2003.

(13) Dewar, M. J. S.; Zoebisch, E. G.; Healy, E. F.; Stewart, J. J. P. Development and Use of Quantum Mechanical Molecular Models. 76. AM1: A New General Purpose Quantum Mechanical Molecular Model. *J. Am. Chem. Soc.* **1985**, *107*, 3902−3909.

(14) Linstrom, P. J.; Mallard, W. G. *NIST Chemistry WebBook, NIST Standard Reference Database Number 69*. National Institute of Standards and Technology: Gaithersburg, MD 20899; 2014.

(15) Braams, B. J.; Bowman, J. M. Permutationally Invariant Potential Energy Surfaces in High Dimensionality. *Int. Rev. Phys. Chem.* **2009**, *28*, 577−606.

(16) Wang, Y.; Bowman, J. M.; Huang, X. Communication: Prediction of the Rate Constant of Bimolecular Hydrogen Exchange in the Water Dimer using an Ab Initio Potential Energy Surface. *J. Chem. Phys.* **2010**, *133*, 111103.

(17) Shank, A.; Wang, Y.; Kaledin, A.; Braams, B. J.; Bowman, J. M. Accurate Ab Initio and "Hybrid" Potential Energy Surfaces, Intramolecular Vibrational Energies, and Classical IR Spectrum of the Water Dimer. *J. Chem. Phys.* **2009**, *130*, 144314.

(18) Braunstein, M.; Conforti, P. F. Classical Dynamics of State-Resolved Hyperthermal $O(^3P)$ + $H_2O(^1A_1)$ Collisions. *J. Chem. Phys.* **2013**, *138*, 074303.

(19) Bonnet, L. Classical Dynamics of Chemical Reactions in a Quantum Spirit. *Int. Rev. Phys. Chem.* **2013**, *32*, 171−228.

(20) Bowman, J. M.; Gazdy, B.; Sun, Q. A Method to Constrain Vibrational Energy in Quasiclassical Trajectory Calculations. *J. Chem. Phys.* **1989**, *91*, 2859−2862.

(21) Miller, W. H.; Hase, W. L.; Darling, C. L. A Simple Model for Correcting Zero Point Energy in Classical Trajectory Simulations of Polyatomic Molecules. *J. Chem. Phys.* **1989**, *91*, 2863−2868.

(22) Schatz, G. C. A Program for Determining Primitive Semiclassical Eigenvalues for Vibrating Rotating Nonlinear Triatomic Molecules. *Comput. Phys. Commun.* **1988**, *51*, 135−147.

(23) Bonnet, L.; Rayez, J. C. Quasiclassical Trajectory Method for Molecular Scattering Processes: Necessity of a Weighted Binning Approach. *Chem. Phys. Lett.* **1997**, *277*, 183−190.

(24) Bonnet, L.; Rayez, J. C. Gaussian Weighting in the Quasiclassical Trajectory Method. *Chem. Phys. Lett.* **2004**, *397*, 106−109.

(25) Czakó, G. Gaussian Binning of the Vibrational Distributions for the Cl + $CH_4(\nu_{4/2} = 0, 1) \rightarrow$ H + $CH_3Cl(n_1n_2n_3n_4n_5n_6)$ Reactions. *J. Phys. Chem. A* **2012**, *116*, 7467−7473.

(26) Czakó, G.; Wang, Y.; Bowman, J. M. Communication: Quasiclassical Trajectory Calculations of Correlated Product-State Distributions for the Dissociation of $(H_2O)_2$ and $(D_2O)_2$. *J. Chem. Phys.* **2011**, *135*, 151102.

(27) Sierra, J. D.; Bonnet, L.; González, M. Quasi-Classical Trajectory−Gaussian Binning Study of the reactions OH + $D_2 \rightarrow$ $HOD(\nu_1',\nu_2',\nu_3')$ + D Angle−Velocity and Vibrational Distributions at a Collision Energy of 2.8 eV. *J. Phys. Chem. A* **2011**, *115*, 7413−7417.

(28) Conte, R.; Fu, B.; Kamarchik, E.; Bowman, J. M.; Novel, A. Gaussian Binning (1GB) Analysis of Vibrational State Distributions in Highly Excited H_2O from Reactive Quenching of OH* by H_2. *J. Chem. Phys.* **2013**, *139*, 044104.

(29) Zittel, P. F. Private communication, 2014.

(30) Kung, R. T. V.; Center, R. E. High Temperature Vibrational Relaxation of H_2O by H_2O, He, Ar, and N_2. *J. Chem. Phys.* **1975**, *62*, 2187−2194.

(31) Cotton, S. J.; Miller, W. H. Symmetrical Windowing for Quantum States in Quasi-Classical Trajectory Simulations. *J. Phys. Chem. A* **2013**, *117*, 7190−7194.

(32) Zittel, P. F.; Masturzo, D. E. Vibrational relaxation of H_2O by H_2, HCl, and H_2O at 295 K. *J. Chem. Phys.* **1991**, *95*, 8005−8012.

(33) Barnes, P. W.; Sims, I. R.; Smith, I. W. M. Relaxation of H_2O from its $|04\rangle^-$ Vibrational State in Collisions with H_2O, Ar, H_2,N_2, and O_2. *J. Chem. Phys.* **2004**, *120*, 5592−5600.

(34) Ramasesha, K.; De Marco, L.; Mandal, A.; Tokmakoff, A. Water Vibrations Have Strongly Mixed Intra- and Intermolecular Character. *Nat. Chem.* **2013**, *5*, 935−940.

DOI: 10.1021/jp5115527
J. Phys. Chem. A XXXX, XXX, XXX−XXX